https://doi.org/10.5194/egusphere-2024-1473
Preprint. Discussion started: 19 June 2024

Optimally solving topography of snow-scaped landscapes to improve snow property retrieval from spaceborne imaging spectroscopy measurements

Brenton A. Wilder[1], Joachim Meyer[1], Josh Enterkine[1], Nancy F. Glenn[1*]
[1]Department of Geosciences, Boise State University, Boise, ID, USA

Correspondence to: Nancy F. Glenn (nancyglenn@boisestate.edu)

Abstract

Accurately modelling snow albedo and specific surface area (SSA) are essential for monitoring the cryosphere in a changing climate and are parameters that inform hydrologic and climate models. These snow surface properties can be modelled from spaceborne imaging spectroscopy measurements but rely on Digital Elevation Models (DEMs) of relatively coarse spatial scales (e.g. Copernicus at 30 m) degrade accuracy due to errors in derived products – like aspect. In addition, snow deposition and redistribution can change the apparent topography and thereby static DEMs may not be considered coincident with the imaging spectroscopy dataset. Testing in three different snow climates (tundra, maritime, alpine), we established a new method that simultaneously solves snow, atmospheric, and terrain parameters, enabling a solution that is more unified across sensors and introduces fewer sources of uncertainty. We leveraged imaging spectroscopy data from AVIRIS-NG and PRISMA (collected within 1 hour) to validate this method and showed a 15% increase in

https://doi.org/10.5194/egusphere-2024-1473
Preprint. Discussion started: 19 June 2024

performance for the radiance-based method versus using the static DEM (from r=0.52 to r=0.60). This concept can be implemented in future missions such as Surface Biology and Geology (SBG) and Copernicus Hyperspectral Imaging Mission for the Environment (CHIME).

Key Words: Imaging Spectroscopy, Snow Properties, Topography, Snow Albedo

1 Introduction

Accurately mapping snow surface properties is essential for seasonal snow zones in a changing climate especially in regions where seasonal snowpack is expected to change dramatically in the coming decades (Siirila-Woodburn et al., 2021). For example, snow albedo plays a crucial role in melting of the snowpack during the ablation season (Wang et al., 2020) with changes in snow albedo directly affecting the amount of absorbed solar radiation, and therefore the amount of snow that is melted off as liquid water. Throughout the winter season, snow albedo fluctuates due in part to grain size (Seidel et al., 2016) and light absorbing particles (Kaspari et al., 2015; McKenzie, 2020; Schmale et al., 2017; Skiles & Painter, 2017). With limited number of *in situ* snow stations around the globe measuring surface properties, and snow surfaces constantly undergoing metamorphism across space and time, satellite imagery represents the best potential for spatial and temporally complete

https://doi.org/10.5194/egusphere-2024-1473
Preprint. Discussion started: 19 June 2024

mapping of snow properties. Accurately retrieving snow albedo and other snow surface properties from satellite imagery is paramount, especially in a rapidly changing climate (Malmros et al., 2018).

Retrieval of snow properties from satellite remote sensing relies on Digital Elevation Models (DEMs) to correct for local terrain effects (Bair et al., 2021; Bair et al., 2022; Dozier et al., 2022). In a previous study, researchers found global DEM products to have "blunders and errors" when compared to airborne lidar, particularly in derived slope and aspect which cause severe errors in calculated solar illumination angles (Dozier et al., 2022). Dozier et al. (2022) found errors in local solar illumination angles ranging from 0.048 to 0.117 across several sites for Copernicus global DEMs caused by errors in slope and aspect. The cosine of the local solar illumination angle, μ_s, is a function (Eq. 1) of slope angle (S), slope aspect (A), solar zenith angle (θ_0), and azimuth angle (ϕ_0) – with the last two being well constrained:

$$\mu_s = \max[0, \cos(\theta_0)\cos(S) + \sin(\theta_0)\sin(S)\cos(\phi_0 - A)] \quad (1)$$

Because θ_0 and ϕ_0 are calculable with low errors (less than 0.05°), the biggest contribution to errors in μ_s stem from slope and aspect. Errors in μ_s increase monotonically with increasing θ_0 (e.g., sun setting has high θ_0, as does solar noon in high latitude winters). This

https://doi.org/10.5194/egusphere-2024-1473
Preprint. Discussion started: 19 June 2024

phenomenon can be explained by plotting Eq. 1 for various solar zenith angles, θ_0, (Figure 1). Put simply, at higher θ_0 there is a higher standard deviation in μ_s surrounding a known slope and aspect (with some temporally consistent uncertainty), increasing the probability and magnitude of such an error. For example, if one were to arbitrarily choose slope and aspect (with some uncertainty), and varying θ_0 (20-70°), one could find a similar range of errors as presented in Dozier et al. (2022).

https://doi.org/10.5194/egusphere-2024-1473
Preprint. Discussion started: 19 June 2024

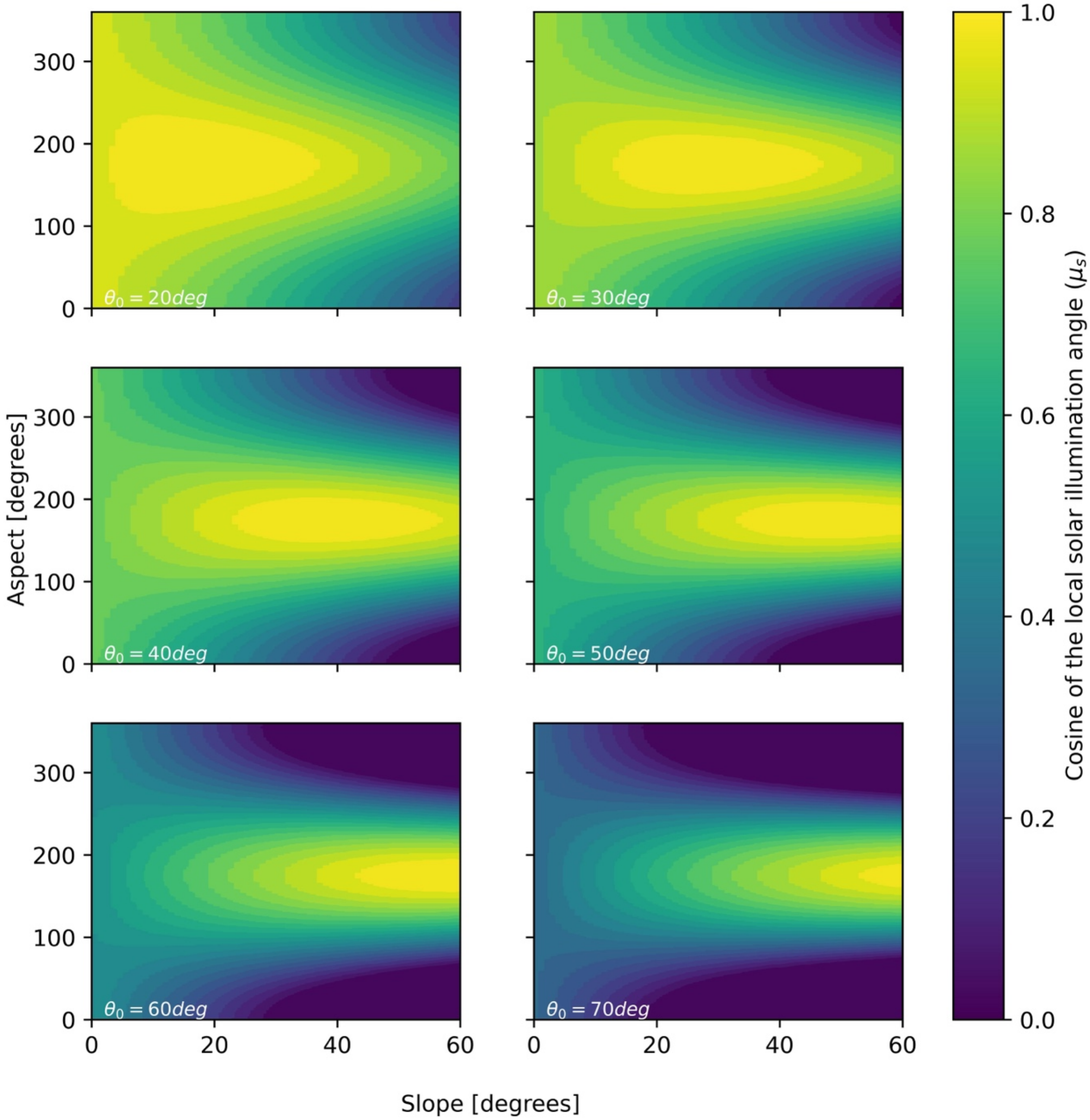

68

69 **Figure 1.** Cosine of local illumination angles (μ_s) as a function of slope (x-axis) and aspect

70 (y-axis) incremented by 1°. Increasing solar zenith angles (θ_0) illustrates the problem at

https://doi.org/10.5194/egusphere-2024-1473
Preprint. Discussion started: 19 June 2024

higher latitude, and/or winter acquisitions, where variability increases with respect to slope and aspect. For this illustration ϕ_0 is fixed at a value of 175°.

Recent work has shown μ_s can be modelled using an optimal estimation framework given the Top of Atmosphere (TOA) radiance observed from imaging spectroscopy (Carmon et al., 2023). The authors solve for surface, atmospheric, and topographic state variables simultaneously in their model. This works physically because the partition of direct to diffuse light introduces a shape and magnitude effect on the TOA radiance spectra. However, retrieving snow optical properties is sensitive to directional reflectance which is significantly influenced by the viewing geometry as well, especially in steep terrain, leading to possible shortcomings in this method specifically for snow covered pixels. To address this and expand upon this framework, we present a new method to account for terrain in snow covered areas. Our method is tested on pixels with greater than 75% snow cover in three different snow climates (tundra, maritime, and alpine) with spaceborne imaging spectroscopy with the aim to reduce error in derived snow properties by optimally solving for topography. The spaceborne results are validated against high confidence airborne spectrometer data and further evaluated with error distributions. This work directly contributes to snow property retrievals in steep terrain and/or at times of high solar illumination angles for upcoming satellite missions such

https://doi.org/10.5194/egusphere-2024-1473
Preprint. Discussion started: 19 June 2024

as Surface Biology and Geology (SBG) (Cawse-Nicholson et al., 2021) and Copernicus Hyperspectral Imaging Mission for the Environment (CHIME) (Celesti et al., 2022).

2 Methods

2.1 Study area

For our study, we used PRecursore IperSpettrale della Missione Applicativa (PRISMA) imagery over three sites capturing different snow climates and solar zenith angles: San Juan Mountains (Colorado, USA, 29 April 2021, θ_0=27°), Mount Shasta (California, USA, 28 February 2021, θ_0=52°), and the Toolik area (Alaska, USA, 21 March 2021, θ_0=68°) (Figure 2). The San Juan Mountains location is considered a high alpine site located in interior continental USA with an elevation range of 2208-4129 m. The Mount Shasta site is a maritime snow climate along the western coast of USA with an elevation range of 750-4232 m. The Toolik site (elevation range = 504-1748m) is a high-latitude tundra site, being mostly flat but with steep sections along the Brooks Range (along the southern part of the image). PRISMA, launched by the Italian Space Agency (ASI) and beginning operation on March 22, 2019, is a spaceborne imaging spectroscopy mission collecting radiance at 30 m spatial resolution across 237 bands spanning 400-2500 nm at a spectral resolution of 9.24 nm and 9.27 nm in the visible-near and shortwave infrared, respectively (Cogliati et al., 2021).

https://doi.org/10.5194/egusphere-2024-1473
Preprint. Discussion started: 19 June 2024

To validate our method, we used four existing Airborne Visible Infrared Imaging Spectrometer-Next Generation (AVIRIS-NG) flightlines over the San Juan Mountains from 29 April 2021 (flying 1 hour after PRISMA acquisition). AVIRIS-NG collects radiance measurements at variable spatial resolution (depending on the flight altitude) across 425 bands spanning 380-2510 nm in 5nm intervals (Green et al., 2023). For this flight, data were collected at 4 m spatial resolution. We downloaded AVIRIS-NG apparent reflectance from National Snow and Ice Data Center (NSIDC) and observation geometry data from NASA Search Earth Data (Skiles & Vuyovich, 2023).

https://doi.org/10.5194/egusphere-2024-1473
Preprint. Discussion started: 19 June 2024

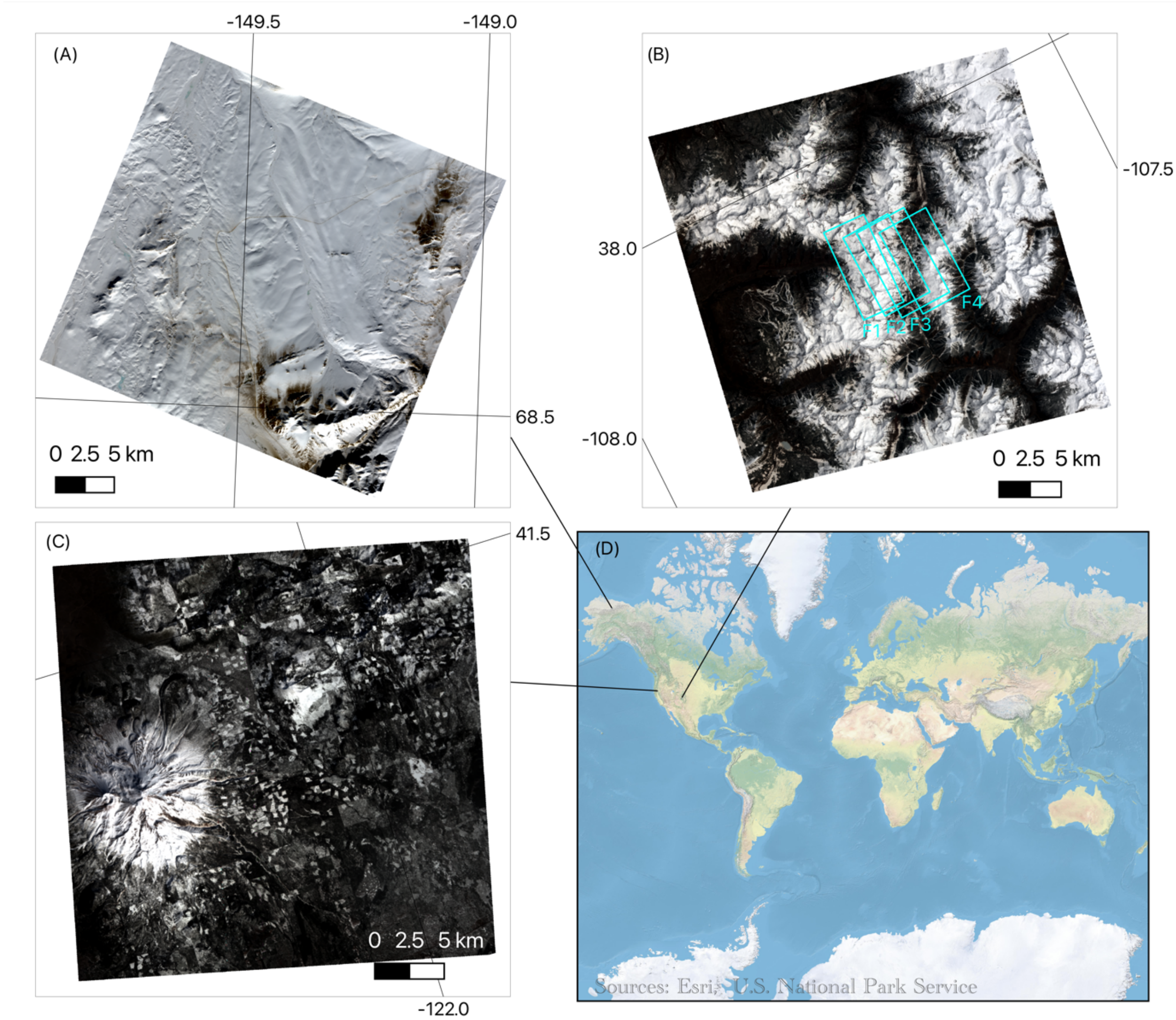

115

116 **Figure 2.** PRISMA true colour images for Toolik on 21 March 2021 (A), San Juan

117 Mountains on 29 April 2021 (B), and Mount Shasta on 28 February 2021 (C). Four

118 coincident AVIRIS-NG flightlines (F1-F4) are shown in cyan over the San Juan Mountains.

119

https://doi.org/10.5194/egusphere-2024-1473
Preprint. Discussion started: 19 June 2024

2.2 Modelling surface, atmosphere, and topography from PRISMA

The algorithmic improvements build off a workflow that estimates snow properties given PRISMA TOA radiance, titled Global Optical Snow properties via High-speed Algorithm using K-means (GOSHAWK) (Wilder et al., 2023; Wilder et al., 2024). In short, GOSHAWK uses the analytic asymptotic radiative transfer model (AART) (Kokhanovsky & Zege, 2004) coupled with libRadtran (Mayer & Kylling, 2005) to invert snow surface and atmospheric properties (Bohn et al., 2021; Dalcin & Fang, 2021), and fractional covers of mixed pixels under varied lighting conditions using non-linear numerical optimization (Bair et al., 2021). The parameters solved for in the optimization routine include fractional covers, specific surface area (SSA), light absorbing particle concentration (modelled as soot), liquid water content (LWC) percentage, dimensionless aerosol optical depth at 550nm, and columnar water vapor in the atmosphere. Here, we expand upon the GOSHAWK algorithm considering recent work showing the capacity to estimate μ_s from TOA radiance (Carmon et al., 2023; Bohn et al. 2024{TBD-preprint..}). This capacity is demonstrated in Figure 3 using fixed snow properties via AART and fixed atmosphere properties via libRadtran across the range of plausible μ_s (i.e. 0 to 1). Like the findings in Carmon et al. (2023), Figure 3 shows that μ_s controls both the spectral shape and magnitude of observed TOA radiance with the effect varying across wavelengths. The greatest shape effect can be seen in the visible spectrum (roughly 400-700 nm) due to the magnitude of the diffuse irradiance. In

https://doi.org/10.5194/egusphere-2024-1473
Preprint. Discussion started: 19 June 2024

combination with the magnitude and shape shift, this parameter becomes solvable during optimization due to its strong separability – especially when considering the entire spectrum data from a hyperspectral remote sensing source such asPRISMA. It is important to note that μ_s impacts both the AART estimation of snow reflectance and libRadtran estimation of incoming solar irradiance.

https://doi.org/10.5194/egusphere-2024-1473
Preprint. Discussion started: 19 June 2024

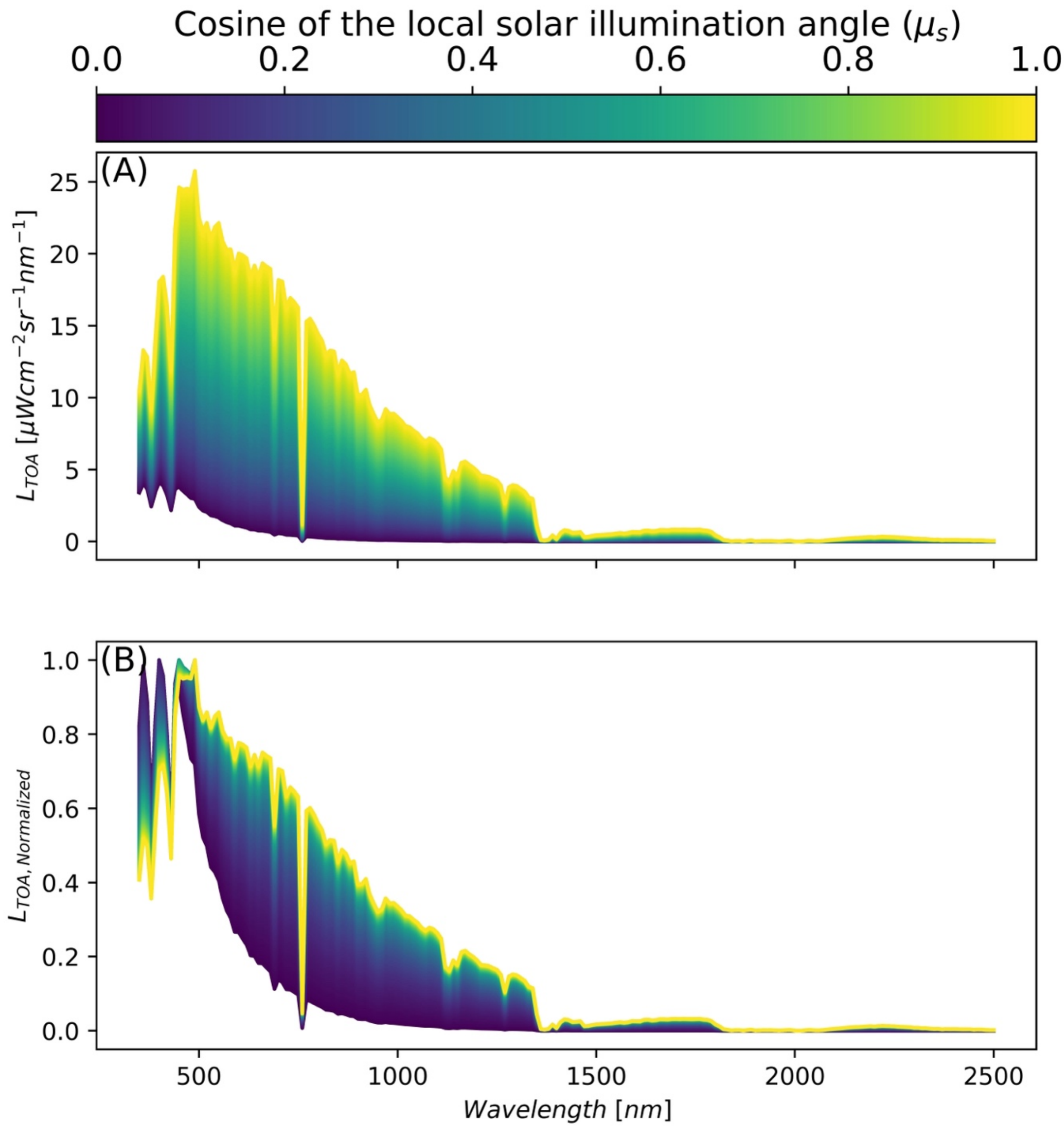

Figure 3. Synthetic data showing change in magnitude (A) and shape (B) of top of atmosphere radiance (L_{TOA}) with respect to changing local solar illumination angle (μ_s) for fixed snow

https://doi.org/10.5194/egusphere-2024-1473
Preprint. Discussion started: 19 June 2024

surface state variables modelled with AART, and fixed atmospheric state variables modelled with libRadtran (viewing geometry was fixed as well). State variables and solar/view geometry were based on a PRISMA acquisition over southern Idaho on 8 December 2022. Figure (B) shows normalized radiance with respect to peak TOA radiance across wavelengths to highlight the change in shape.

However, if we were only to optimize μ_s, the other key terms, local viewer zenith angle (μ_v) and local phase angle (ξ) in the AART formulation for bidirectional reflectance of snow (Kokhanovsky & Zege, 2004) would remain constant from the available DEM (i.e., μ_s, μ_v, ξ are all derived from DEM) (Eq. 2; Wilder et al., 2024),

$$r_{snow}(\mu_s, \mu_v, \xi, \lambda) = r0(\mu_s, \mu_v, \xi)\ \alpha_{snow}(\lambda) \tag{2}$$

where $r0$ represents the semi-infinite nonabsorbing snow layer, α_{snow} is the plane albedo, and r_{snow} is the bidirectional reflectance of snow. Keeping other terms $\mu_v\ and\ \xi$ the same are problematic because snow reflectance is poorly approximated as a non-Lambertian surface (Leroux & Fily, 1988), and the outcome will be greatly influenced by $\mu_v\ and\ \xi$. Therefore, to incorporate solving for μ_s, μ_v, $and\ \xi$ from TOA radiance into the GOSHAWK algorithm, we instead elect to optimally solve for cos(aspect) (i.e., “northness”) and sin(aspect) (i.e.,

https://doi.org/10.5194/egusphere-2024-1473
Preprint. Discussion started: 19 June 2024

"eastness") (Table 1). Aspect can be solved during optimization by using the atan2 function (Van Rossum, 2020). We chose to use this method because eastness and northness are continuously differentiable, and therefore, are suited for numerical optimization methods, whereas aspect is circular. We then can use this optimal aspect to estimate μ_s (Eq. 1), μ_v (Eq. 3), and ξ (Eq. 4),

$$\mu_v = \max[0,\ \cos(\theta_v)\cos(S) + \sin(\theta_v)\sin(S)\cos(\phi_v - A)] \quad (3)$$

$$\xi = \cos^{-1}(-\mu_s\mu_v + sin(\theta_i)\, sin(\theta_v)\, cos(180 - (\phi_v - \phi_0))) \quad (4)$$

where ϕ_v is the viewing azimuth angle, and θ_v is the viewer zenith angle on a flat plane. This directly impacts Eq. 5 and the formulation of incoming solar energy in the model,

$$E(\lambda) = \psi\mu_s E(\lambda)_{dir} + V_\Omega E(\lambda)_{diff} + \left[\left(1 + \frac{\cos(S)}{2} - V_\Omega\right) r(\lambda)_{surf}\left(E(\lambda)_{dir} + E(\lambda)_{diff}\right)\right] \quad (5)$$

where E is total incoming irradiance, ψ is binary shade or no shade, E_{dir} and E_{diff} are the direct and diffuse irradiance, respectively, V_Ω is the sky view factor, and r_{surf} is the reflectance of nearby terrain. Explicitly within GOSHAWK the following equation is then solved using non-linear numerical optimization (Wilder et al., 2024). Adding in the two extra parameters

https://doi.org/10.5194/egusphere-2024-1473
Preprint. Discussion started: 19 June 2024

in our updated optimization scheme did not change our run time significantly, which still hovered around 15 minutes (depending on the image), as noted in Wilder et al. (2024). It is also worth noting that while the optimal aspect cannot be solved accurately due to a non-unique solution space (Figure 1), the resulting μ_s, μ_v , and ξ are unique and the solution is such. Rasters of SSA and LWC at the surface were developed to verify this algorithm update.

https://doi.org/10.5194/egusphere-2024-1473
Preprint. Discussion started: 19 June 2024

205 **Table 1.** Parameter space and initial vectors used in numerical optimization.

Parameter [unit]	Definition	Feasible Range	Initial State	Type
f-snow [%]	Fractional snow in the mixed pixel	[0, 100]	10	Surface
f-shade [%]	Fractional shade in the mixed pixel	[0, 100]	20	Surface
f-LC1 [%]	Fractional cover of endmember 1 (based on land cover value at pixel)	[0, 100]	50	Surface
f-LC2 [%]	Fractional cover of endmember 2 (based on land cover value at pixel)	[0, 100]	20	Surface
SSA [m^2 kg^{-1}]	Specific surface area, which is related to the optical grain size at the snow surface via the density of ice	[2, 156]	40	Surface
LAP [ng g^{-1}]	Concentration of light absorbing particles, modelled as soot.	[0, 0.5e-5]	0	Surface
LWC [%]	Percentage of liquid water content in the snowpack.	[0, 50]	2	Surface
AOD 550 [%]	Dimensionless Aerosol Optical Depth at 550 nm	[1,100]	10	Atmospheric
H_2O [mm]	Columnar water vapor in the atmosphere	[1,50]	1	Atmospheric
Eastness	sin(aspect)	[-1,1]	Variable	Topographic
Northness	cos(aspect)	[-1,1]	Variable	Topographic

https://doi.org/10.5194/egusphere-2024-1473
Preprint. Discussion started: 19 June 2024

2.2 Estimating snow properties from AVIRIS-NG for validation

Due to the higher signal to noise ratio and the higher spatial resolution of AVIRIS-NG, we treated the dataset as the ground reference. It also captured a similar spectral range to PRISMA which made it a suitable comparison dataset. To select snow-covered pixels, we solved for NDSI (Normalized Difference Snow Index) using bands at 600 nm and 1500 nm. We limited our retrieval for NDSI greater than or equal to 0.90 (Painter et al., 2013). A common approach to retrieve snow grain size from pure snow pixels is to apply the scale band area algorithm (Nolin & Dozier, 2000); however, it is recognized that large presence of LWC is a limitation. The maximum air temperature of 10.8° C on the day of the image at the San Juan Mountains site indicated that elevated LWC at the surface was probable (Center for Snow and Avalanche Studies, 2023). Additionally, reflectance spectra appeared to be shifted along the x-axis (wavelength) due to the presence of LWC. Therefore, we used numerical optimization to model apparent snow reflectance with AART by allowing fractional shade, LWC, and SSA to vary. We did not include rock or forest endmembers in this formulation, assuming the 4 m pixels are relatively homogenous. Topographic incident angles were held constant based on the 4 m resolution DEM provided by AVIRIS-NG. We minimized Root Mean Square Error (RMSE) between observed-apparent and modelled-apparent snow reflectance from AART wavelengths greater than 900 nm and not impacted by atmospheric

https://doi.org/10.5194/egusphere-2024-1473
Preprint. Discussion started: 19 June 2024

interference and LAP (Miller et al. 2016) (901-1299 nm, 1451-1779 nm, and 1951-2449 nm). The presence of LWC was included in our analysis by means of the composite refractive index of water and ice (Donahue et al., 2022; Segelstein, 1981; Warren & Brandt, 2008).

2.4 Comparing modelled snow albedo and SSA

The GOSHAWK algorithm was used in two different modes: 1) static topography based on the Copernicus DEM (hereon called "***static***"); and 2) solved topography based on the algorithm updates (hereon called "***radiance***"). To compare the accuracy of PRISMA derived SSA and LWC, we resampled the AVIRIS-NG results to match the PRISMA resolution (30 m) and extents by using bilinear interpolation. Then, we sampled all valid pixels where PRISMA and AVIRIS-NG had snow. We then computed r-pearson correlation coefficient, Mean Bias, and RMSE for the radiance and static methods (with respect to AVIRIS-NG). Finally, we used Copernicus derived slope and aspect maps to determine where the largest errors were occurring on the landscape to compare with the theoretical basis presented in Figure 1. We do this by using the Mean Absolute Error (MAE) with respect to slope and aspect. We expected to see higher differences in north facing aspects (i.e., μ_s approaches 0), and where θ_0 was higher. To test the interaction with θ_0 more fully, we extended the analysis to Mount Shasta, CA, and Toolik, Alaska, where no in *situ data*

https://doi.org/10.5194/egusphere-2024-1473
Preprint. Discussion started: 19 June 2024

existed. Finally, we compared the modelled broadband albedo and SSA between the radiance and static methods to assess how these assumptions propagated into outputs.

3 Results

3.1 Validation using AVIRIS-NG data over the San Juan Mountains

When comparing the two methods over each pixel in the AVIRIS-NG flightlines (Figure 4) we found that the radiance method performed better for SSA and LWC (Table 2). The greatest improvement over the static DEM method was observed where average SSA was highest (flightline f1), with RMSE improving from 15.58 m^2 kg^{-1} to 11.12 m^2 kg^{-1}. Interestingly, across all flightlines the radiance method had a lower range in RMSE (8.66 - 11.12 m^2 kg^{-1}) compared to the static method (RMSE was 8.99-15.58 m^2 kg^{-1}). Over all flightlines, AVIRIS-NG estimated SSA = 23.23 +/- 13.18 m^2 kg^{-1}, PRISMA radiance method estimated SSA = 23.67 +/- 12.45 m^2 kg^{-1}, and PRISMA static method estimated SSA = 25.06 +/- 16.06 m^2 kg^{-1}.

There was a consistent negative bias of 0.10-0.11 for LWC estimates from both static and radiance when compared to AVIRIS-NG. Despite the bias, r ranged from 0.48-0.65 depending on the flightline and method, showing a strong signal of LWC present at the site. The average LWC for the entire study area was estimated by AVIRIS-NG at 0.17 +/- 0.06, PRISMA radiance method at 0.07 +/- 0.07, and PRISMA static method at 0.05 +/-0.05. As

https://doi.org/10.5194/egusphere-2024-1473
Preprint. Discussion started: 19 June 2024

previously noted, the temperatures were well above freezing during the overpass of AVIRIS-NG and occurred roughly 1 hour later in the day compared to the PRISMA acquisition. This most likely explains the higher LWC observed by AVIRIS-NG.

https://doi.org/10.5194/egusphere-2024-1473
Preprint. Discussion started: 19 June 2024

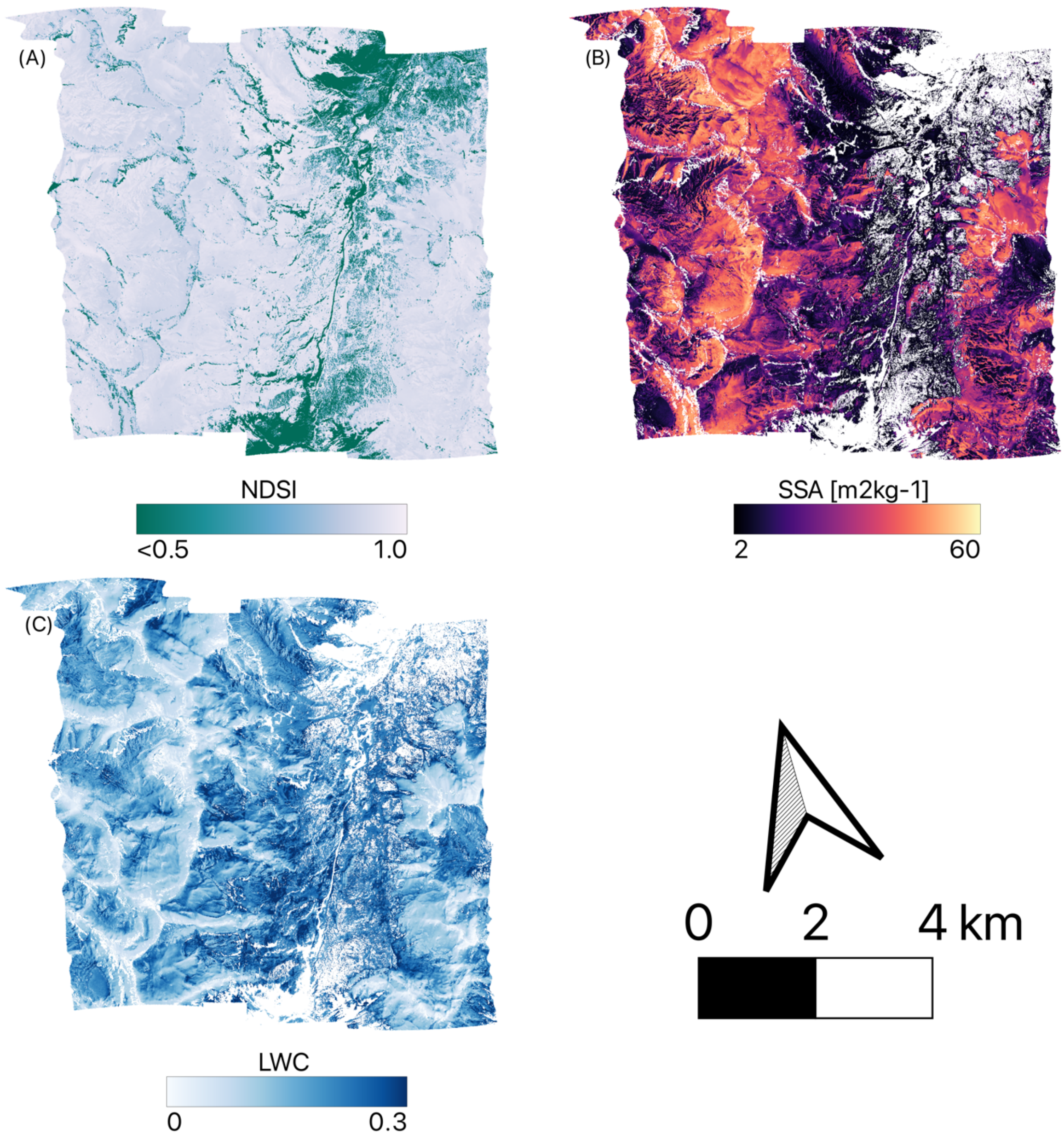

265

https://doi.org/10.5194/egusphere-2024-1473
Preprint. Discussion started: 19 June 2024

Figure 4. Snow properties computed from AVIRIS-NG (4 m spatial resolution) on 29 April 2021 including NDSI (A), SSA (B), and LWC (C) for the San Juan Mountain site.

Table 2. Performance metrics of the static and radiance methods deriving SSA (m^2 kg^{-1}) and LWC from PRISMA imagery over the area of the AVIRIS-NG bounds. The two methods are compared to AVIRIS-NG derived values as ground truth.

		SSA (m^2 kg^{-1})			LWC [0-1]		
AVIRIS-NG Flightline	PRISMA Method	RMSE	Average Bias	r	RMSE	Average Bias	r
f1 n=16,171	Static	15.58	0.01	0.38	0.12	-0.11	0.57
	Radiance	11.12	-1.08	0.49	0.12	-0.11	0.54
f2 n=12,930	Static	12.15	-4.33	0.57	0.12	-0.11	0.65
	Radiance	10.13	-4.00	0.66	0.11	-0.10	0.62
f3 n=5,722	Static	10.27	1.86	0.52	0.12	-0.10	0.51
	Radiance	9.12	2.33	0.57	0.12	-0.10	0.48
f4 n=8,292	Static	8.99	2.00	0.70	0.12	-0.11	0.57
	Radiance	8.66	3.10	0.73	0.11	-0.10	0.54

https://doi.org/10.5194/egusphere-2024-1473
Preprint. Discussion started: 19 June 2024

Combined f1-f4	Static	13.10	-0.57	0.52	0.12	-0.11	0.62
	Radiance	10.25	-0.67	0.60	0.12	-0.11	0.60

The error analysis revealed large outliers modelled by the static method (Figure 5) when compared to the reference AVIRIS-NG SSA. This can be seen in Figure 5b as a long tail of the density histograms for the static method. These errors primarily occurred on steep, north facing aspects (e.g., when μ_s approached 0). Using a moving average with respect to μ_s, radiance derived SSA followed the general distribution of AVIRIS-NG derived SSA much better, even as μ_s approached 0. This differs from the static method where the modelled SSA and resulting RMSE from inversion begin to diverge as μ_s approached 0.

https://doi.org/10.5194/egusphere-2024-1473
Preprint. Discussion started: 19 June 2024

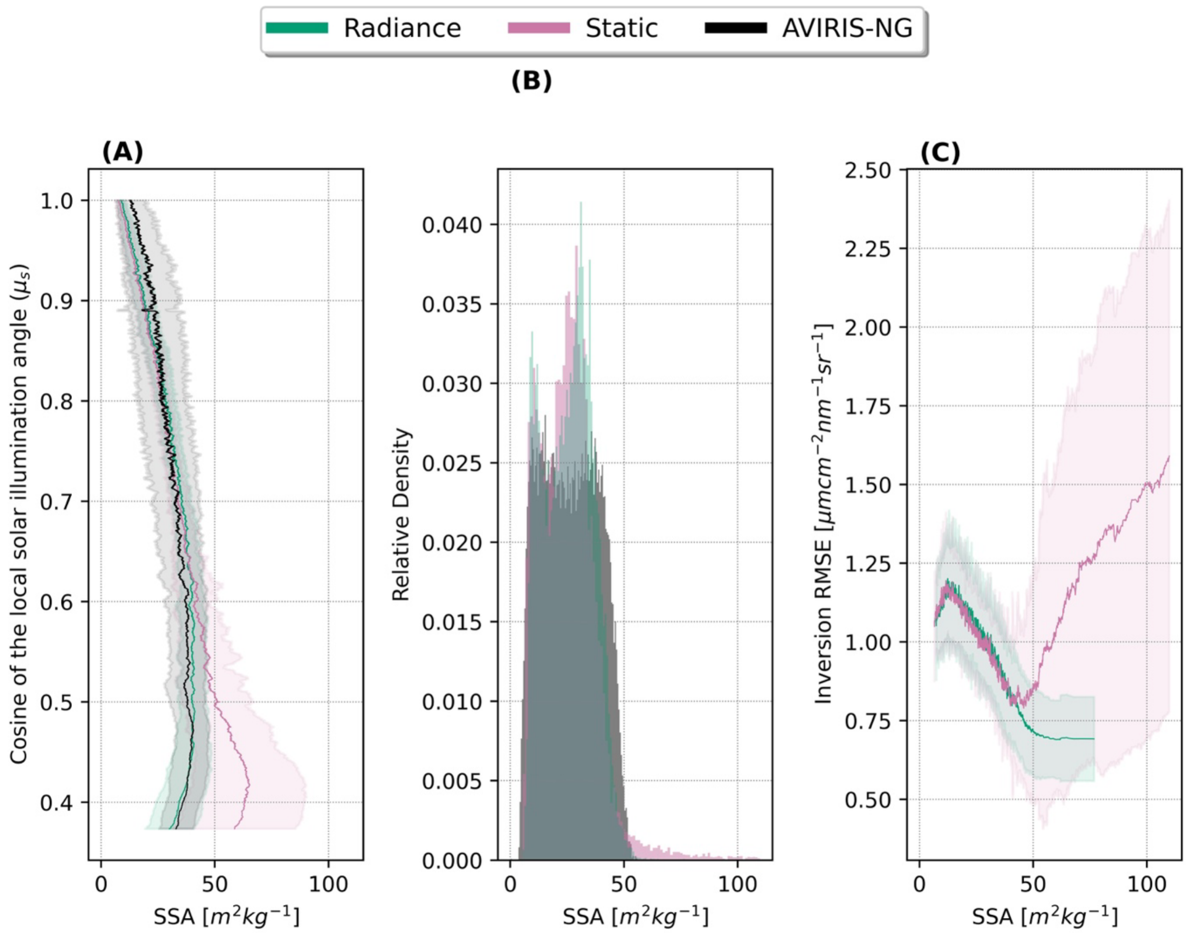

Figure 5. Modelled SSA for radiance method (green), static method (pink), and AVIRIS-NG (black) with respect to μ_s (A), modelled SSA density histogram (B), and resulting RMSE from the inversion from PRISMA with respect to solved SSA (C). Note that panels (A) and (C) are plotted using a moving average and binned with respect to μ_s and SSA, respectively.

https://doi.org/10.5194/egusphere-2024-1473
Preprint. Discussion started: 19 June 2024

Next, we found the radiance method error (MAE = 8.19 m^2 kg^{-1}) was more evenly distributed across the entire landscape (combined flightlines 1 through 4) (Figure 6). This is unlike the static method, where symmetric zones of larger error can be seen that are similar to the theoretical approach in Figure 1. Similarly, we found absolute error increased as μ_s approached zero for the static method ($r = 0.27$; $p<0.01$), while this relationship was not evident for the radiance method ($r = -0.04$; $p<0.01$).

https://doi.org/10.5194/egusphere-2024-1473
Preprint. Discussion started: 19 June 2024

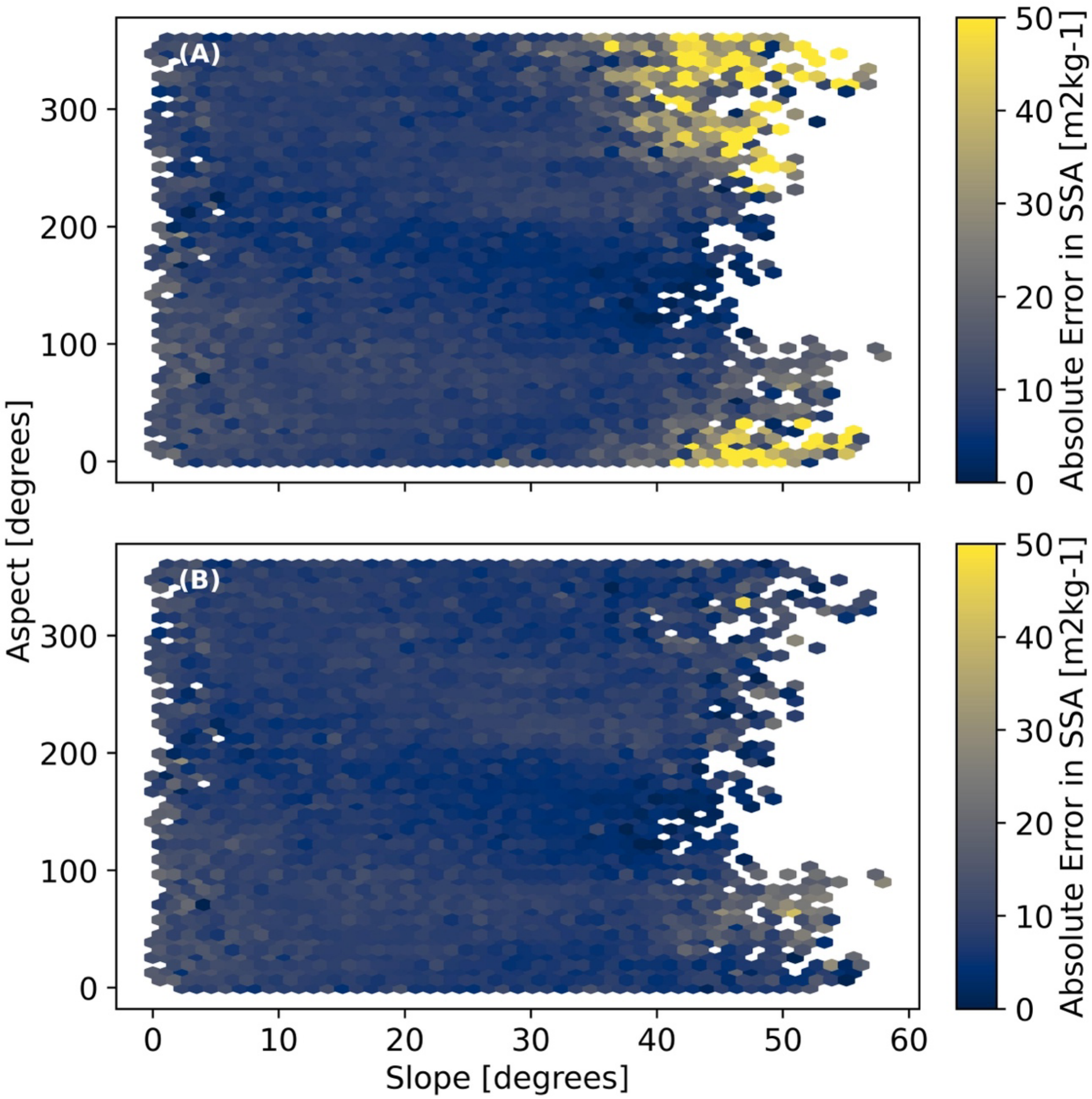

Figure 6. 2D Histogram showing absolute error in SSA compared to AVIRIS-NG with respect to slope and aspect across the entire dataset for PRISMA static method (A), and PRISMA radiance method (B). Absolute error is calculated as |PRISMA SSA – AVIRIS-NG SSA|.

https://doi.org/10.5194/egusphere-2024-1473
Preprint. Discussion started: 19 June 2024

3.2 Comparing radiance and static methods between sites

On average for the Mount Shasta site, the radiance method estimated SSA was 17.57 +/- 14.58 $m^2\ kg^{-1}$, and static method SSA was 17.74 +/- 12.67 $m^2\ kg^{-1}$ (Table 3). Notably, there were more data gaps in the static method, resulting from failed inversions likely due to errors in the slope and aspect. On average for the Toolik site the radiance method estimated SSA to be 51.50 +/- 12.46 $m^2\ kg^{-1}$, and the static method estimated 52.07 +/- 14.49 $m^2\ kg^{-1}$.

https://doi.org/10.5194/egusphere-2024-1473
Preprint. Discussion started: 19 June 2024

Table 3. Image-wide statistics of SSA and broadband albedo between the two methods (static vs. radiance) processing the PRISMA imagery for all three sites.

Site	PRISMA Method	Mean SSA (m^2 kg^{-1})	Standard Deviation of SSA (m^2 kg^{-1})	Mean Broadband Albedo	Standard Deviation of Broadband Albedo
San Juan	Static	22.14	19.40	0.79	0.03
	Radiance	21.27	15.94	0.78	0.04
Shasta	Static	17.74	12.67	0.74	0.05
	Radiance	17.57	14.58	0.72	0.06
Toolik	Static	52.07	14.49	0.82	0.03
	Radiance	51.50	12.46	0.81	0.03

Additionally, we saw the highest difference between the two methods on north facing aspects, where μ_s approached 0 (Figure 7). The difference in distributions matched closely to the theoretical demonstration (Figure 1) and is most likely associated with the standard error of slope and aspect from Copernicus DEM given the illumination conditions. This result demonstrated that the difference between the two methods had the biggest impact for images where θ_0 was high.

https://doi.org/10.5194/egusphere-2024-1473
Preprint. Discussion started: 19 June 2024

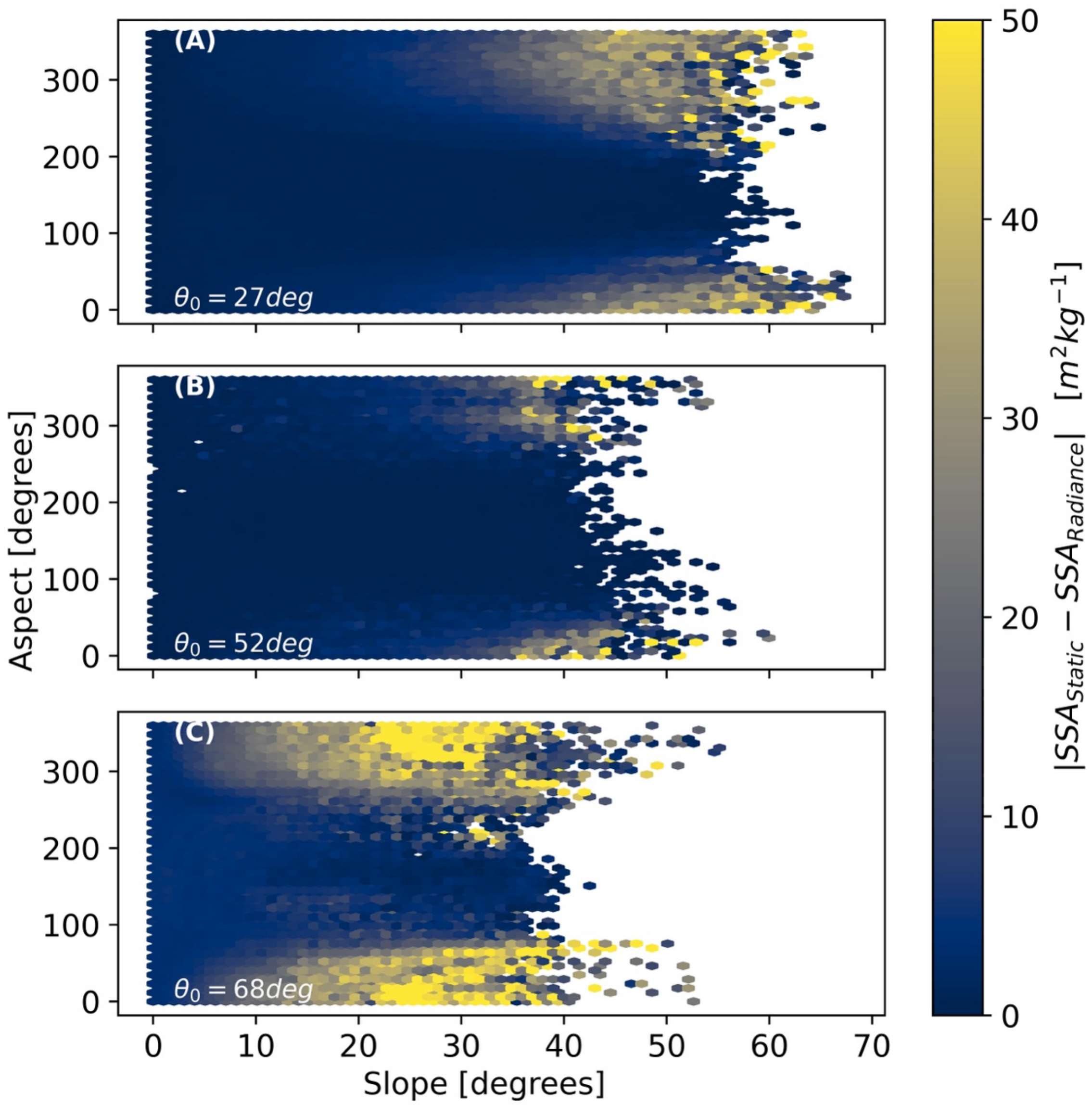

Figure 7. 2D Histogram plot showing absolute error in SSA with respect to slope and aspect across the entire dataset, treating radiance method as validation, absolute difference is

https://doi.org/10.5194/egusphere-2024-1473
Preprint. Discussion started: 19 June 2024

calculated as |Static – Radiance|. This is shown for the San Juan Mountains site (A), Shasta site (B), and Toolik site (C). The average solar zenith angle ($\boldsymbol{\theta_0}$) is shown for reference on each panel.

We observed a small but notable difference between the methods in derived snow broadband albedo (BA) values (Figure 8). On average the standard deviation between BA_{Static} – $BA_{Radiance}$ (δBA) for the San Juan Mountains site was 0.02, standard deviation for the Shasta site was 0.01, and standard deviation for the Toolik site was 0.02. Generally, there was not a clear bias with respect to μ_s. For the San Juan Mountains site, most of the pixels from the static method showed a consistent small, negative bias of around -0.002. However, for shadier slopes at this site, this bias flipped positive and was much more uncertain at around +0.02. Interestingly, δBA from the Toolik site had the opposite relationship to San Juan Mountains site, where δBA was more positive on sunnier slopes (μ_s approaching 1), and more negative on shadier slopes (μ_s approaching 0), suggesting there could be different mechanisms for which the static method may lead to inaccuracies. The result for the Toolik site confirms the need to model the illumination conditions even in relatively flat terrain, because of implications for net radiative forcing in the cryosphere. The Mount Shasta site δBA had no strong relationship with respect to μ_s.

https://doi.org/10.5194/egusphere-2024-1473
Preprint. Discussion started: 19 June 2024

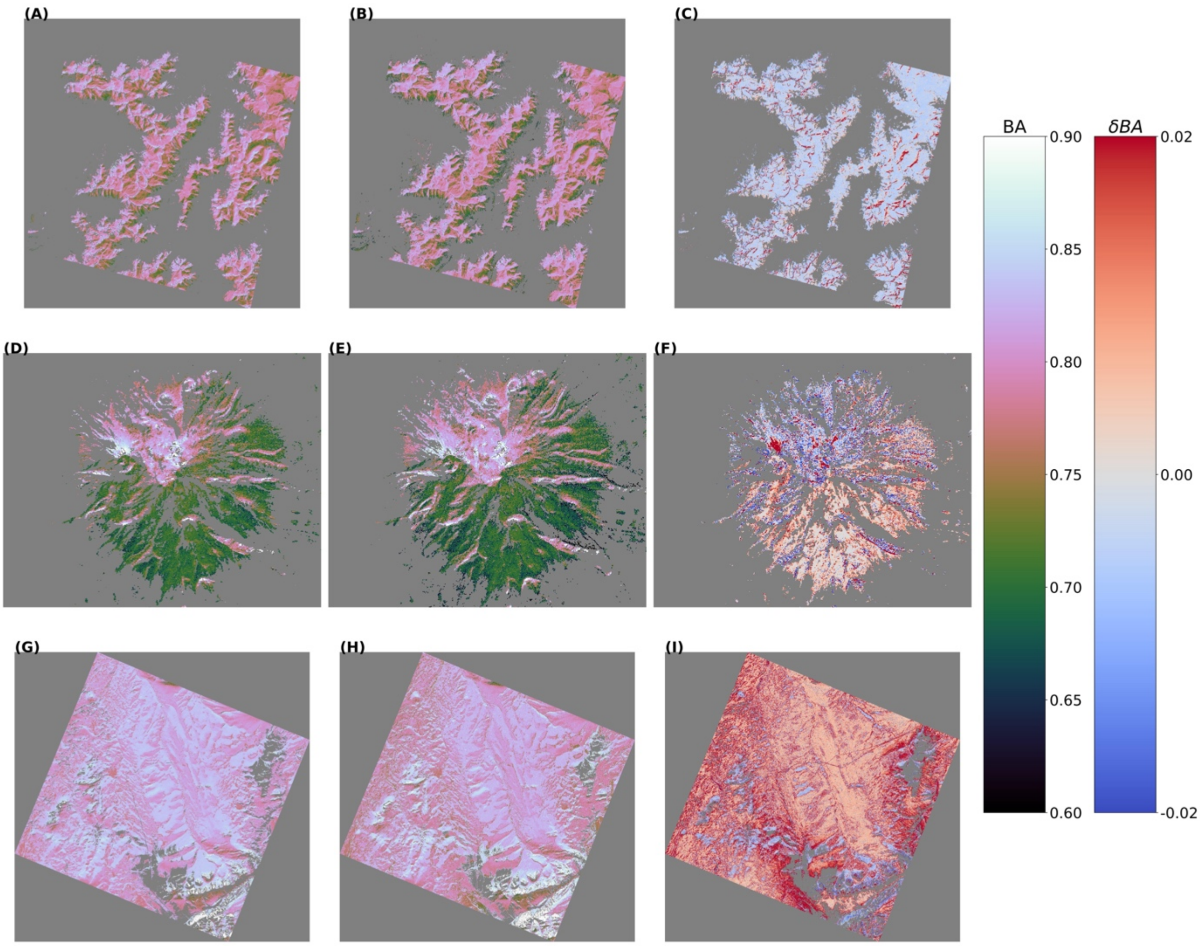

Figure 8. Modelled broadband snow albedo (BA) for San Juan Mountains site (A-C), Shasta Mountain site (D-F), and Toolik site (G-I). Left column represents BA from static method, middle column represents BA from radiance method, and right column represents difference in BA (δBA), which is $BA_{Static} - BA_{Radiance}$. Dark grey colour symbolizes data that is not a value.

https://doi.org/10.5194/egusphere-2024-1473
Preprint. Discussion started: 19 June 2024

When plotting moving average of |δBA| for all sites with respect to $\boldsymbol{\mu_s}$ we found that generally |δBA| increased as $\boldsymbol{\mu_s}$ approached zero (Figure 9). However, this relation appeared highly non-linear and depended on the site and illumination conditions. For example, standard deviation of |δBA| (shown as the shaded regions in Figure 9) for well-lit slopes ($\boldsymbol{\mu_s} > \mathbf{0.8}$) were generally smaller for San Juan site, and conversely were higher for the Toolik site. Similar to Dozier et al. (2022), one can see a monotonic relation with respect to $\boldsymbol{\theta_0}$ across the three sites. This exercise demonstrates the levels of uncertainty left in for static DEM methods, further showing quantitatively the improvements to broadband albedo through using radiance-based approach.

https://doi.org/10.5194/egusphere-2024-1473
Preprint. Discussion started: 19 June 2024

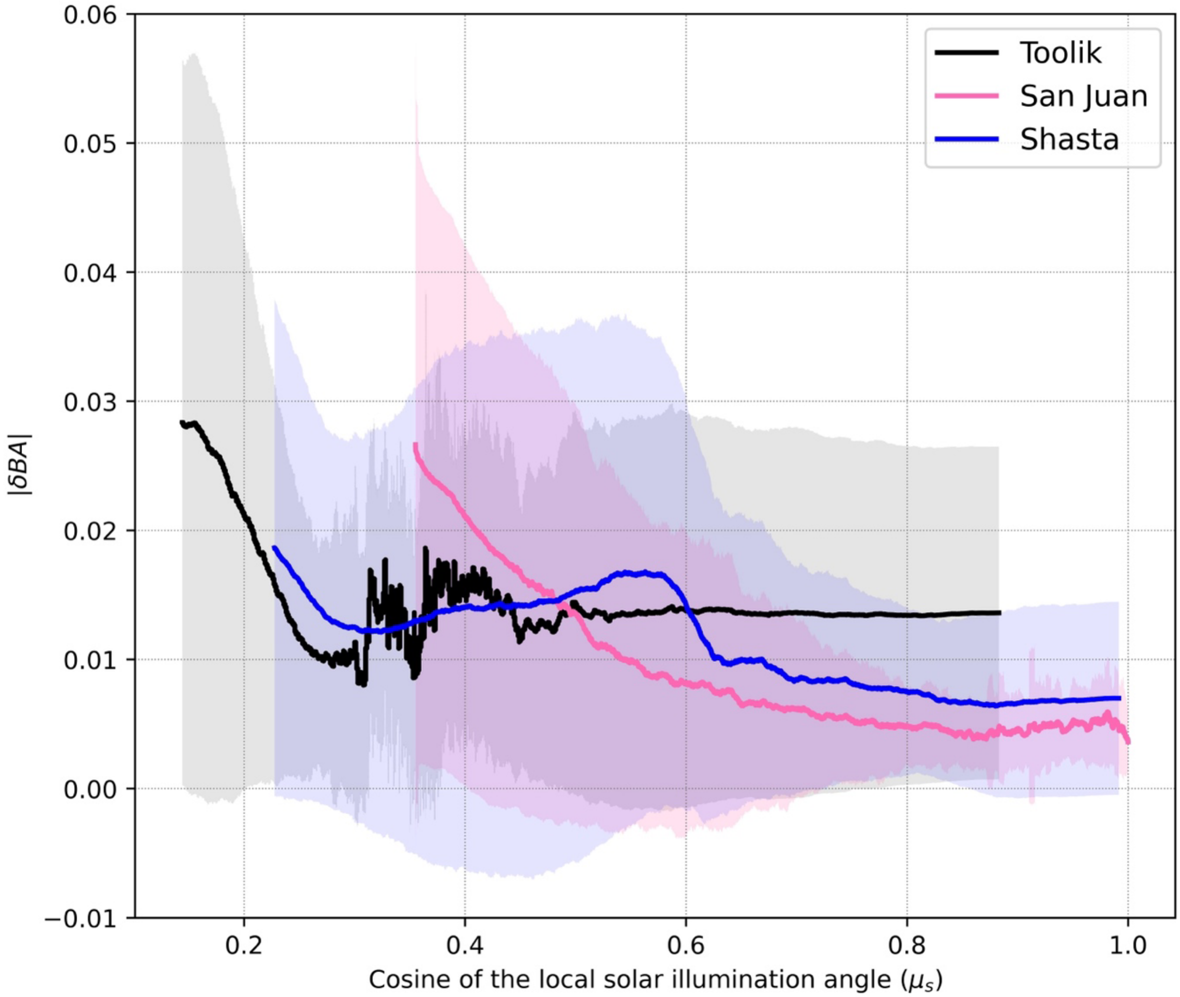

Figure 9. Modelled absolute difference in broadband albedo ($|\delta BA| = |BA_{Static} - BA_{Radiance}|$) for Toolik (black), San Juan (pink), and Shasta (blue). Note these are plotted using a moving average and binned with respect to $\boldsymbol{\mu_s}$.

https://doi.org/10.5194/egusphere-2024-1473
Preprint. Discussion started: 19 June 2024

4 Discussion

4.1 Implications in accounting for terrain in snow property retrieval

Derivative slope and aspect maps are prone to errors at 30 m spatial resolutions (Dozier et al., 2022), which become relevant for derived snow products from upcoming missions such as SBG and CHIME which will rely on such topographic information to calculate optical properties like snow albedo so that we can better monitor seasonal snowmelt. These errors can be inherent to the DEM itself, or a product of spatial and temporal misalignments (Carmon et al., 2023). To enable high quality snow products regardless of illumination angles and conditions, we have demonstrated benefits of computing optimal terrain using TOA radiance over snow. This new method is especially useful for steep mountain terrain and/or high latitudes where illumination conditions are suboptimal. The θ_0 (solar zenith angle) was relatively low for the San Juan Mountain site in our study, and thus represents a lower bound of the improvement in accuracy one could expect (Figure 1; Dozier et al., 2022). This disparity was demonstrated further for the Mount Shasta and Toolik sites when θ_0 was larger (i.e. a greater differences in SSA due to more challenging solar and sensor geometry). Even for the relatively flat Toolik site, we showed that correctly accounting for incidence angels can have an impact when θ_0 is large. Our modelled δBA with respect to the non-coincident DEM was similar to work by Donahue et al. (2023), who found similar uncertainties of δBA (ranging from -10 to 10%) for their

https://doi.org/10.5194/egusphere-2024-1473
Preprint. Discussion started: 19 June 2024

investigation on Place Glacier, British Columbia, Canada. We corroborated with this research showing similar ranges of δBA for our three study sites.

This research responds to the objectives stated in "*Thriving on our changing planet: A decadal strategy for Earth observation from space",* to improve biogeophysical modelling at scales driven by topography (National Academies of Sciences, Engineering, & Medicine, 2019), enabling more accurate snow property retrievals in the cryosphere under challenging illumination conditions. Our work presented on solving terrain where DEM data are not available or reliable may serve to accelerate improvements to satellite remote sensing tools to monitor and model at both the regional global scale (Sturm et al., 2017), at a critical juncture in time where northern latitudes are changing fast under a warming climate.

4.2 Future considerations

While we solved for a few terrain parameters in this study, we did entirely remove the static DEM, even from the radiance method. The elevation from a DEM has a much higher confidence than its derivative products (Dozier et al., 2022). Therefore, we used these values to inform our atmospheric routine, as well as our shadow casting ray tracing module in GOSHAWK (Wilder et al., 2024). Additionally, as stated in Wilder et al. (2024), GOSHAWK used the Dozier & Frew (1981) method for estimating the sky view factor (V_Ω) based on nearby terrain. This factor could potentially be problematic but was cited as being

https://doi.org/10.5194/egusphere-2024-1473
Preprint. Discussion started: 19 June 2024

not as important as μ_s (Dozier et al., 2022). Therefore, we elected to use V_Ω derived from the static Copernicus DEM. However, this could be an area for future improvement, especially in very steep terrain where V_Ω becomes small.

Finally, we used a static value for slope derived from Copernicus DEM. The slope influences the μ_s term, but also influences the passive radiation from nearby slopes. Ultimately, we concluded that aspect had the largest impact on changing μ_s (Figure 1), as well as large RMSE reported in previous work (Dozier et al., 2022; Donahue et al., 2023), and thus was the focus of our study. However, future work could investigate other model and optimization configurations to improve upon this study. We recommend additional coincident AVIRIS-NG flights with spaceborne imaging spectroscopy datasets to further this work.

5 Conclusions

In this study we have used existing PRISMA imagery to demonstrate the improvements in modelling snow optical properties when explicitly modelling the terrain in the inversion. This presents an interesting concept, that end users who are interested in modelling snow from space, are perhaps better off working with the L1 TOA products, and not using the L2 bottom of atmosphere reflectance products space agencies typically produce. This would especially be true for areas where the surface undergoes rapid change, such as on glaciers. A final thought to consider is the creation of snow optical mapping using a combination of PRISMA, CHIME, SBG, etc. – and that in performing the operation in this way you may create unified snow products that have the same terrain and atmospheric uncertainties.

Code Availability. https://github.com/cryogars/goshawk

Author contributions. B.W. created the GOSHAWK algorithm and updates herein, decided on experiment set-up, and performed the subsequent analysis, as well as being the main article writer. J.M., J.E. and N.G. provided ideas, comments, and supervised the work.

Competing interests. The contact author has declared that neither they nor their co-authors have any competing interests.

Acknowledgements. We acknowledge the Italian Space Agency (ASI) for providing us access to PRISMA imagery and providing us the foundational data necessary for this research. We thank Dr. McKenzie Skiles for aiding us in modelling the snow properties from AVIRIS-NG, and for supplying the dataset.

Financial support. This research has been supported by FINESST Award – 21-EARTH21-0249.

https://doi.org/10.5194/egusphere-2024-1473
Preprint. Discussion started: 19 June 2024

References

1. Bair, E. H., Dozier, J., Stern, C., LeWinter, A., Rittger, K., Savagian, A., … & Davis, R. E. (2022). Divergence of apparent and intrinsic snow albedo over a season at a sub-alpine site with implications for remote sensing. *The Cryosphere*, *16*(5), 1765-1778.

2. Bair, E. H., Stillinger, T., & Dozier, J. (2021). Snow property inversion from remote sensing (SPIReS): A generalized multispectral unmixing approach with examples from MODIS and Landsat 8 OLI. *IEEE Transactions on Geoscience and Remote Sensing*, *59*, 7270–7284. https://doi.org/10.1109/TGRS.2020.3040328

3. Board, S. S., & National Academies of Sciences, Engineering, and Medicine. (2019). *Thriving on our changing planet: A decadal strategy for Earth observation from space*. National Academies Press.

4. Bohn, N., Painter, T. H., Thompson, D. R., Carmon, N., Susiluoto, J., Turmon, M. J., ... & Guanter, L. (2021). Optimal estimation of snow and ice surface parameters from imaging spectroscopy measurements. *Remote Sensing of Environment*, *264*, 112613.

5. Carmon, N., Berk, A., Bohn, N., Brodrick, P. G., Dozier, J., Johnson, M., ... & Susiluoto, J. (2023). Shape from spectra. *Remote Sensing of Environment*, *288*, 113497.

https://doi.org/10.5194/egusphere-2024-1473
Preprint. Discussion started: 19 June 2024

6. Cawse-Nicholson, K., Townsend, P. A., Schimel, D., Assiri, A. M., Blake, P. L., Buongiorno, M. F., ... & SBG Algorithms Working Group. (2021). NASA's surface biology and geology designated observable: A perspective on surface imaging algorithms. *Remote Sensing of Environment*, *257*, 112349.

7. Celesti, M., Rast, M., Adams, J., Boccia, V., Gascon, F., Isola, C., & Nieke, J. (2022, July). The Copernicus Hyperspectral Imaging Mission for the Environment (Chime): Status and Planning. In *IGARSS 2022-2022 IEEE International Geoscience and Remote Sensing Symposium* (pp. 5011-5014). IEEE.

8. Center for Snow and Avalanche Studies (2023). Archival Data from Senator Beck Basin Study Area. https://snowstudies.org/archived-data/

9. Chlus, A., Gierach, M., & Townsend, P. A. (2022). EnSpec/sister: 1.0.0 (1.0.0). Zenodo. https://doi.org/10.5281/zenodo.5997779

10. Cogliati, S., Sarti, F., Chiarantini, L., Cosi, M., Lorusso, R., Lopinto, E., ... & Colombo, R. (2021). The PRISMA imaging spectroscopy mission: Overview and first performance analysis. *Remote sensing of environment*, *262*, 112499.

11. Dalcin, L., & Fang, Y. L. L. (2021). mpi4py: Status update after 12 years of development. *Computing in Science & Engineering*, *23*(4), 47-54.

https://doi.org/10.5194/egusphere-2024-1473
Preprint. Discussion started: 19 June 2024

12. Donahue, C., Skiles, S. M., & Hammonds, K. (2022). Mapping liquid water content in snow at the millimeter scale: an intercomparison of mixed-phase optical property models using hyperspectral imaging and in situ measurements. *The Cryosphere*, *16*(1), 43-59.

13. Donahue, C. P., Menounos, B., Viner, N., Skiles, S. M., Beffort, S., Denouden, T., ... & Heathfield, D. (2023). Bridging the gap between airborne and spaceborne imaging spectroscopy for mountain glacier surface property retrievals. *Remote Sensing of Environment*, *299*, 113849.

14. Dozier, J., & Frew, J. (1981). Atmospheric corrections to satellite radiometric data over rugged terrain. *Remote Sensing of Environment*, *11*, 191-205.

15. Dozier, J., Bair, E. H., Baskaran, L., Brodrick, P. G., Carmon, N., Kokaly, R. F., … & Thompson, D. R. (2022). Error and Uncertainty Degrade Topographic Corrections of Remotely Sensed Data. *Journal of Geophysical Research: Biogeosciences*, *127*(11), e2022JG007147.

16. European Space Agency. (2021). Copernicus Global Digital Elevation Model [Dataset]. Distributed by Open Topography. https://doi.org/10.5069/G9028PQ

https://doi.org/10.5194/egusphere-2024-1473
Preprint. Discussion started: 19 June 2024

17. Green, R. O., Brodrick, P. G., Chapman, J. W., Eastwood, M., Geier, S., Helmlinger, M., ... & Thorpe, A. K. (2023). AVIRIS-NG L2 Surface Reflectance, Facility Instrument Collection, V1. ORNL DAAC, Oak Ridge, Tennessee, USA.
18. Kaspari, S., McKenzie Skiles, S., Delaney, I., Dixon, D., & Painter, T. H. (2015). Accelerated glacier melt on Snow Dome, Mount Olympus, Washington, USA, due to deposition of black carbon and mineral dust from wildfire. *Journal of Geophysical Research: Atmospheres*, *120*(7), 2793-2807.
19. Kokhanovsky, A. A., & Zege, E. P. (2004). Scattering optics of snow. *Applied optics*, *43*(7), 1589-1602.
20. Kokhanovsky, A. A. (2021). The Broadband Albedo of Snow. *Frontiers in Environmental Science*, *9*, 757575.
21. Leroux, C., & Fily, M. (1998). Modeling the effect of sastrugi on snow reflectance. *Journal of Geophysical Research: Planets*, *103*(E11), 25779-25788.
22. Malmros, J. K., Mernild, S. H., Wilson, R., Tagesson, T., & Fensholt, R. (2018). Snow cover and snow albedo changes in the central Andes of Chile and Argentina from daily MODIS observations (2000–2016). *Remote Sensing of Environment*, *209*, 240-252.

https://doi.org/10.5194/egusphere-2024-1473
Preprint. Discussion started: 19 June 2024

23. Mayer, B., & Kylling, A. (2005). The libRadtran software package for radiative transfer calculations-description and examples of use. *Atmospheric Chemistry and Physics*, *5*(7), 1855-1877.

24. McKenzie, Donald. (2020). Mountains in the Greenhouse: Climate Change and the Mountains of the Western U.S.A.. 10.1007/978-3-030-42432-9.

25. Miller, S.D., Wang, F., Burgess, A.B., Skiles, S.M., Rogers, M. and Painter, T.H., 2016. Satellite-based estimation of temporally resolved dust radiative forcing in snow cover. *Journal of Hydrometeorology*, *17*(7), pp.1999-2011.

26. O'Neel, S., Wilder, B., Keskinen, Z., Zikan, K. H., Enterkine, J., Filiano, D. L., ... & Adebisi, N. (2022, December). Helicopter-Borne Lidar to Resolve Snowpack Variability in Southwest Idaho. In *AGU Fall Meeting Abstracts* (Vol. 2022, pp. C35E-0922).

27. Painter, T. H., Seidel, F. C., Bryant, A. C., McKenzie Skiles, S., & Rittger, K. (2013). Imaging spectroscopy of albedo and radiative forcing by light-absorbing impurities in mountain snow. *Journal of Geophysical Research: Atmospheres*, *118*(17), 9511-9523.

28. Segelstein, D. J. (1981). *The complex refractive index of water*(Doctoral dissertation, University of Missouri--Kansas City).

https://doi.org/10.5194/egusphere-2024-1473
Preprint. Discussion started: 19 June 2024

29. Seidel, F. C., Rittger, K., Skiles, S. M., Molotch, N. P., & Painter, T. H. (2016). Case study of spatial and temporal variability of snow cover, grain size, albedo and radiative forcing in the Sierra Nevada and Rocky Mountain snowpack derived from imaging spectroscopy. *The Cryosphere*, *10*(3), 1229-1244.

30. Siirila-Woodburn, E. R., Rhoades, A. M., Hatchett, B. J., Huning, L. S., Szinai, J., Tague, C., ... & Kaatz, L. (2021). A low-to-no snow future and its impacts on water resources in the western United States. *Nature Reviews Earth & Environment*, *2*(11), 800-819.

31. Skiles, S. M., & Painter, T. (2017). Daily evolution in dust and black carbon content, snow grain size, and snow albedo during snowmelt, Rocky Mountains, Colorado. *Journal of Glaciology*, *63*(237), 118-132.

32. Skiles, M. and C. M. Vuyovich. (2023). SnowEx21 Senator Beck Basin and Grand Mesa, CO AVIRIS-NG Surface Spectral Reflectance, Version 1 [Data Set]. Boulder, Colorado USA. NASA National Snow and Ice Data Center Distributed Active Archive Center. https://doi.org/10.5067/ZAI3M64WWN5V. Date Accessed 02-09-2024.

33. Sturm, M., Goldstein, M. A., & Parr, C. (2017). Water and life from snow: A trillion dollar science question. *Water Resources Research*, *53*(5), 3534-3544.

https://doi.org/10.5194/egusphere-2024-1473
Preprint. Discussion started: 19 June 2024

34. U.S. Geological Survey, 2019, 3D Elevation Program 1-Meter Resolution Digital Elevation Model (published 20200606), accessed June 1, 2023 at URL https://www.usgs.gov/the-national-map-data-delivery

35. Van Rossum, G. (2020). *The Python Library Reference, release 3.8.2*, Python Software Foundation.

36. Wang, W., Yang, K., Zhao, L., Zheng, Z., Lu, H., Mamtimin, A., ... & Moore, J. C. (2020). Characterizing surface albedo of shallow fresh snow and its importance for snow ablation on the interior of the Tibetan Plateau. *Journal of Hydrometeorology*, *21*(4), 815-827.

37. Warren, S. G., & Brandt, R. E. (2008). Optical constants of ice from the ultraviolet to the microwave: A revised compilation. *Journal of Geophysical Research: Atmospheres*, *113*(D14).

38. Wilder, B. A., Glenn, N. F., Lee, C. M., Marshall, H. P., Brandt, J., Kinoshita, A. M., ... & Enterkine, J. (2023, July). Global Optical Snow properties via High-speed Algorithm With K-means clustering (GOSHAWK). In *IGARSS 2023-2023 IEEE International Geoscience and Remote Sensing Symposium*(pp. 118-120). IEEE.

39. Wilder, B. A., Lee, C. M., Chlus, A., Marshall, H. P., Brandt, J., Kinoshita, A. M., ... & Glenn, N. F. (2024). Computationally efficient retrieval of snow surface properties from spaceborne imaging spectroscopy measurements through dimensionality

https://doi.org/10.5194/egusphere-2024-1473
Preprint. Discussion started: 19 June 2024

reduction using k-means spectral clustering. *IEEE Journal of Selected Topics in Applied Earth Observations and Remote Sensing*.